

# Fast and Reliable Estimation of Multiple Parametric Images Using an Integrated Method for Dynamic SPECT

Lingfeng Wen\*, *Member, IEEE*, Stefan Eberl, *Member, IEEE*, Dagan Feng, *Fellow, IEEE*, Weidong Cai, *Member, IEEE*, and Jing Bai, *Fellow, IEEE*

**Abstract**—Dynamic single photon emission computed tomography (SPECT) has demonstrated the potential to quantitatively estimate physiological parameters in the brain and the heart. The generalized linear least square (GLLS) method is a well-established method for solving linear compartment models with fast computational speed. However, the high level of noise intrinsic in the SPECT data leads to reliability and instability problems of GLLS for generating parametric images. An integrated method is proposed to restrict the noise in both the temporal and spatial domains to estimate multiple parametric images for dynamic SPECT. This method comprises three steps which are optimum image sampling schedule in the projection space, cluster analysis applied postreconstruction and parametric image generation with GLLS. The simulation and experimental studies for the neuronal nicotine acetylcholine receptor tracer of 5-<sup>123</sup>I-iodo-A-85380 were employed to evaluate the performance of the proposed method. The results of influx rate of  $K_1$  and volume of distribution of  $V_d$  demonstrated that the integrated method was successful in generating low noise parametric images for high noise SPECT data without enhancing the partial volume effect. Furthermore, the integrated method is computationally efficient for potential clinical applications.

**Index Terms**—Clustering methods, parameter estimation, sampling methods, single photon emission computed tomography (SPECT).

## I. INTRODUCTION

POSITRON emission tomography (PET) and single photon emission computed tomography (SPECT) can measure physiological processes and metabolism *in vivo*. The high

Manuscript received July 13, 2006; revised October 24, 2006. This work was supported in part by the Australian Research Council, in part by the University Grants Committee of Hong Kong, in part by the National Natural Science Foundation of China, and in part the National Basic Research Program of China. *Asterisk indicates corresponding author.*

\*L. Wen was with the Department of Biomedical Engineering, Tsinghua University, 100084 Beijing, China. He is now with the School of Information Technologies, University of Sydney, Sydney, NSW 2006 Sydney, Australia and also with the Department of PET and Nuclear Medicine, Royal Prince Alfred Hospital, NSW 2050 Sydney, Australia. (e-mail: wenlf@ieee.org).

S. Eberl is with Department of PET and Nuclear Medicine, Royal Prince Alfred Hospital, NSW 2050 Sydney Australia and with School of Information Technologies, University of Sydney, NSW 2006 Sydney, Australia (e-mail: stefan@cs.usyd.edu.au).

D. Feng is with School of Information Technologies, University of Sydney, NSW 2006 Sydney, Australia and also with the Center for Multimedia Signal Processing, Department of Electronic and Information Engineering, Hong Kong Polytechnic University, Kowloon, Hong Kong (e-mail: feng@cs.usyd.edu.au).

W. Cai is with School of Information Technologies, University of Sydney, NSW 2006 Sydney, Australia (e-mail: tomc@it.usyd.edu.au).

J. Bai is with Department of Biomedical Engineering, Tsinghua University, 100084 Beijing, China (e-mail: deabj@tsinghua.edu.cn).

Digital Object Identifier 10.1109/TMI.2006.889708

sensitivity and ease of quantification have traditionally favored PET for providing absolute physiological parameter estimates. With appropriate attenuation and scatter correction, quantitative physiological parameter estimation has also been demonstrated with multi-detector gamma camera systems and dynamic SPECT in the brain and the heart [1]–[4].

The process of estimating physiological parameters from functional imaging data consists of acquiring dynamic projection data and measuring the tracer concentration in blood/plasma over the duration of the study to provide the input function (IF). The dynamic projection data sets are quantitatively reconstructed and tissue time activity curves (TTACs) derived from the reconstructed data are fitted, together with the IF, to an appropriate model describing the kinetics of the tracer. TTACs are typically generated from manually or semi-automatically defined regions of interest (ROIs). Averaging across the voxels in the ROI restricts noise in the TTACs and makes it suitable for fitting to the model using nonlinear least squares fitting. However, it is often advantageous to generate parametric images of the physiological process of interest, which then no longer restricts the quantitative analysis to the defined ROIs.

Nonlinear least squares (NLS) and nonlinear weighted least squares (NWLS) methods are considered as the methods of choice for providing parameter estimates for TTACs derived from ROIs with optimum statistical accuracy. However, NLS and NWLS are not well suited to fitting TTACs from individual voxels for parametric image generation due to their high computational burden and proneness to be trapped in local minima when fitting the noisy voxel-based TTACs, particularly when the initial parameters estimates are not close to the correct solution [5]. Graphical approaches are commonly employed to generate parametric images through linear or multilinear regression analysis of parameter estimates [6]–[10]. Patlak *et al.* proposed a graphical method to estimate the influx rate constant  $K_i$  [7], which is directly related to metabolic rate of glucose consumption (MRGlc) for the irreversible FDG model. Logan extended the graphical analysis to the reversible compartment model with particular emphasis on receptor studies in the brain [8]. In receptor studies, the need for blood sampling to derive the IF can be avoided if a reference tissue can be identified with similar nonspecific binding as the regions of interest, but which is devoid of the receptors of interest [6], [9]. However, graphical analysis provides only a limited number of parameters, typically no more than two. Furthermore, some assumptions in graphical methods may give rise to bias in the parametric images.

The generalized linear least square (GLLS) method has been proposed as a computationally efficient method to estimate individual kinetic parameters and physiological parameters without the need to specify initial parameters [11]–[13]. Thus, GLLS is potentially suitable to generate parametric images from dynamic SPECT studies. However, even for multidetector systems, the sensitivity of SPECT is still at least an order of magnitude lower than that achievable in PET, which leads to a high level of noise. High levels of noise can result in reliability and instability problems with GLLS, such as negative rate constant estimates, which are clearly not physiologically correct. A strategy involving noise reduction in both the temporal and spatial domains is proposed to improve the reliability of GLLS for estimating parametric images from dynamic SPECT studies. The proposed method is evaluated with simulation and experimental studies for the neuronal nicotinic acetylcholine receptor tracer of 5- $^{123}\text{I}$ -iodo-A-85380.

## II. METHODS

### A. Integrated Method

The high levels of noise in SPECT data can prove challenging in the estimation of parametric images. The aim of the proposed method is to reduce noise efficiently without adversely impacting on quantitative accuracy. The proposed integrated method is composed of optimum image sampling schedule (OISS) in the projection space and cluster analysis applied post-reconstruction, followed by parametric image generation using GLLS.

1) *OISS of the Projection Data*: High frame rates, particularly immediately after tracer injection, have been recommended for conventional sampling schedule (CSS) to avoid bias [14], [15]. However, this results in very poor counting statistics and noisy data, particularly for the early period with short frames. OISS has been found to improve signal-to-noise ratio (SNR) for PET studies, by decreasing the number of frames required to estimate the parameters of interest, without adverse impact on the accuracy of the parameter estimates [16]–[18]. More recently, OISS has been validated successfully for ROI based analysis of dynamic SPECT neuroreceptor studies [19]. Therefore, the first step of the integrated method applies OISS to determine the optimum frame rate for the projection data.

OISS is determined by iteratively optimizing the cost function of  $\Phi$  (1) with consecutive sampling intervals adjusted

$$\Phi = \text{Max} \left( \sum_{i=1}^n |M_i| \right) \quad (1)$$

where  $n$  is the total number of cortical structures of interest with high affinity for the tracer,  $M_i$  represented the Fisher information matrix of the model parameters for the  $i$ th structure.

Starting from one given sampling schedule, such as the conventional sampling schedule, the cost function is maximized iteratively by adjusting and combining adjacent sampling intervals, while keeping the total study duration constant. Once OISS is obtained for a particular tracer's kinetics, it is then applied to all studies for that particular tracer, i.e., OISS does not have to be redefined for each individual study with that particular tracer.

2) *Cluster Analysis of Reconstructed Data*: The number of different kinetics which can be expected from the different structures in the brain is finite and hence TTACs from a particular structure or mixtures of structures due to partial volume effects should be similar, and the observed differences can be attributed to noise. According to this assumption, the noisy SPECT data can be represented by a limited number of curves representing the kinetics observed for the different structures, while still maintaining quantitative accuracy. Cluster analysis is one multivariate analysis technique with the aim to classify and organize the information into relatively homogeneous groups. Cluster analysis has been applied to process dynamic PET data [20], [21] and for image segmentation [22]. Therefore, the integrated method includes cluster analysis as the second step to reduce noise in the spatial domain. While there are many methods of cluster analysis for different imaging modalities [23], [24], the integrated method employs simple cluster analysis using a weighted least-square distance measure (2) between the candidate voxel and cluster centroid

$$E(z_i, \bar{u}_j) = \sum_{t=1}^p w_t [z_i(t) - \bar{u}_j(t)]^2 \quad (2)$$

In (2),  $z_i(t)$  represents the TTAC for the  $i$ th voxel in reconstructed data,  $\bar{u}_j(t)$  is the centroid TTAC of the  $j$ th cluster, and  $p$  is the total number of frames. The centroid TTAC is the mean curve of all the voxel TTACs belonging to the particular cluster. The weight function  $\mathbf{w} = \{w_1, w_2, \dots, w_p\}$  was chosen to be proportional to the frame durations divided by the whole scan duration, with higher weights for frames with longer collection times and hence better counting statistics.

The TTACs for each voxel are used to generate the weighted least-square distances for each of all the obtained clusters  $C_A$ , followed by derivation of minimum weighted least-square distance with corresponding  $k$ th cluster as shown in (3). The voxel is then classified automatically into the nearest cluster  $C_k$  with the minimum weighted least-square distance according to the criterion (4)

$$\forall j \in C_A : E(z_i, \bar{u}_k) \leq E(z_i, \bar{u}_j) \\ \Rightarrow \min(E(z_i, \bar{u}_j)) = E(z_i, \bar{u}_k) \quad (3)$$

$$\min(E(z_i, \bar{u}_j)) < \Delta d \Rightarrow z_i \in C_k \quad (4)$$

where  $\Delta d$  is the threshold to determine whether TTAC of candidate  $z_i$  satisfies the maximum allowable weighted least-square distance requirement. The threshold is determined as follows: the four-dimensional (three-dimensional space plus one-dimensional time) image data are converted to three-dimensional data by summing the weighted time frames for each voxel, using the same weight  $\mathbf{w}$  as above. An intensity histogram is then formed from these data. The histogram bins representing background voxels and bins containing less than 10 voxels are automatically removed from the derived histogram. The threshold is then calculated from the remaining histogram range by dividing the range by a constant factor found empirically to be 5 for this investigation. The resultant bin number is then multiplied by the bin size to give the threshold in terms of temporally summed counts.

If the threshold criterion is met, the corresponding voxel is added to cluster  $C_k$ . Otherwise, a new cluster is formed to represent this voxel which does not fulfill the similarity requirements for any known cluster centroids. The clusters' centroid TTACs are updated to reflect the contribution from different or additional TTACs when cluster memberships are varied. The cluster analysis is iterated, to minimize misclassification of particular voxels assigned early to clusters, but are then found to be more appropriately assigned to different clusters, due to changing cluster centroids as more voxels are added to or removed from the cluster.

The cluster centroids established at the previous iteration are used to assign voxels to clusters for the current iteration based on the similarity between the voxel and cluster centroid TTACs. Theoretically, the cluster analysis has to be iterated until cluster centroid TTACs no longer vary between iterations. However, in some cases, the cluster analysis does not meet the above criterion of stable cluster centroid TTACs even with a very high number of iterations. Therefore, the approach adopted in this paper is to stop the iterative cluster analysis when the number of clusters no longer changes during the iterations. In general, about one hundred iterations of the cluster analysis were required for the simulation data and clinical data in this paper.

3) *Parameter Estimates*: GLLS has been found useful in nonuniformly and uniformly sampled biomedical signal processing and parameter estimation [11]–[13]. Unbiased parameters can be obtained by GLLS through linearization of the differential equations without the need to specify initial parameters. In the third step of the integrated method, GLLS is used to estimate the individual parameters for the obtained cluster centroid TTACs. To generate the voxel-by-voxel parametric images, all voxels belonging to a particular cluster are assigned the parameter values obtained from the corresponding cluster centroid TTAC. Thus for a parametric image derived by the integrated method, the number of piecewise constant parameter values is equal to the number of clusters from the cluster analysis.

For comparison, parametric images were also generated using established graphical methods. The volume of distribution image of three-compartment and four-parameter model was estimated from the slope of the Logan plot [8] as shown in (5), after allowing sufficient time for equilibrium to be reached and the term “*Con*” to be constant

$$Y_1(t) = V_d \cdot X_1(t) + Con \quad (5)$$

where

$$Y_1(t) = \frac{\int_0^t C_i(t) \cdot dt}{C_i(t)}$$

$$X_1(t) = \frac{\int_0^t C_p(t) \cdot dt}{C_i(t)}$$

$$V_d = \frac{K_1}{k_2} \left( 1 + \frac{k_3}{k_4} \right).$$

Parametric images of the influx rate constant  $K_1$  of the two-compartment and two-parameter model were generated using the Yokoi method [10] as in

$$Y_2(t) = -k_2 \cdot X_2(t) + K_1 \quad (6)$$

where

$$Y_2(t) = \frac{C_i(t)}{\int_0^t C_p(t) \cdot dt}$$

$$X_2(t) = \frac{\int_0^t C_i(t) \cdot dt}{\int_0^t C_p(t) \cdot dt}.$$

Given the different underlying models applied in the graphical methods i.e., two-compartment model for Yokoi method and three-compartment model for Logan plot, the corresponding identical kinetic models were used in the GLLS estimation, i.e., a two-compartment, two-parameter model for  $K_1$  and a three-compartment, four-parameter model for  $V_d$ .

### B. Computer Simulation

Monte Carlo simulations of projection data were performed to compare the performance of the integrated method with that of the traditional graphical techniques for the generation of parametric images at various levels of noise. High count static projection data for individual structures of the brain were simulated for  $^{123}\text{I}$  with the SimSET Monte Carlo package [25] based on the Zubal mathematical human brain phantom [26] to obtain approximately noise-free projection data. The effects of attenuation, scatter, limited detector and collimator spatial resolutions, and energy resolution were included in the simulation. The collimator parameters for the simulations were based on the low-energy high-resolution (LEHR), parallel hole collimators of Triad XLT triple head gamma camera (Trionix Research Laboratories, Twinsburg, OH). An energy window of 20% centered around 159 keV for  $^{123}\text{I}$  was assumed and the energy resolution was based on that measured on the Triad XLT gamma camera (10%). The SimSET Monte Carlo package uses an analytical model for the collimator, rather than fully simulating the collimator as part of the Monte Carlo photon transport. Thus, the model of the collimator was extended by assuming that the penetration of the high-energy photons of  $^{123}\text{I}$  through the LEHR collimator septa adds constant background counts to the projection data as proposed by Iida *et al.* [27]. The high energy photon background was assumed to be a fraction (0.16) of the total counts in the brain, with the fraction determined from brain studies performed on the Triad XLT camera with  $^{123}\text{I}$ .

To validate the Monte Carlo simulation, static planar images were acquired for a line source filled with  $^{123}\text{I}$  with the same Triad XLT triple head gamma camera fitted the LEHR collimators. The line source was 300-mm-long and 1-mm-diameter and contained 33.1 MBq of  $^{123}\text{I}$  and was located in the center of field of view (FOV) of the camera. The distance of the detector to line source was 50, 100, 150, and 200 mm, respectively, for the first four studies. A water tank containing 100-mm-deep water was interposed between the line source and the detector in the fifth study and the distance of detector to the line source was 200 mm. A total of 500 thousand counts were obtained for each study. The projection matrix was  $256 \times 256$  with pixel size of  $1.27 \times 1.27$  mm. Monte Carlo simulations of the same line source geometries were carried out according to the simulation procedure of the brain phantom.

Kinetic parameters and a plasma time activity curve from our previous studies with the tracer 5- $^{123}\text{I}$ -iodo-A-85380 [28]

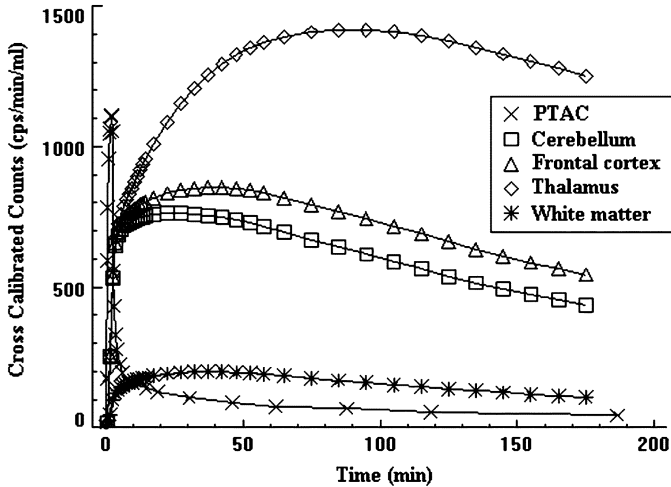


Fig. 1. Plasma and tissue time activity curves for the frontal cortex, thalamus, cerebellum, and white matter. Plasma time activity curve (PTAC).

were employed to generate TTACs for the main brain structures of interest (see Fig. 1). Dynamic projections were generated for each structure, by multiplying the static projections by the value from the corresponding TTAC for the structure for each of the frames defined by the sampling schedule. The dynamic projections from each of the structures were summed to provide a composite dynamic projection data set combining all brain structures.

The background counts from the penetration of high energy photons of  $^{123}\text{I}$  were added to the summed dynamic projection data as detailed above. The projection data sets were scaled to appropriate pixel counts typical to those obtained in the experimental studies for the tracer to allow addition of realistic Poisson noise. Dynamic projection data sets with five different levels of Poisson noise were generated based on maximum pixel counts for a 5-min frame ranging from 30 to 50 counts/pixel to allow effect of noise to be investigated over the range of noise which can be expected in clinical studies with the tracer 5- $^{123}\text{I}$ -iodo-A-85380. A projection data set without noise added was also generated for comparison.

The dynamic projection data sets were scatter corrected by transmission dependent scatter correction [2], [3] and septal penetration of the high energy photons was corrected by adding a constant background term to the scatter correction [27]. The scatter corrected data were reconstructed with the ordered subsets expectation-maximization (OS-EM) iterative reconstruction method [29] using 20 subsets and two iterations and attenuation corrected with an attenuation coefficient map appropriate for  $^{123}\text{I}$  derived from the mathematical phantom. Resolution recovery or other forms of partial volume corrections were not included in the reconstruction or data processing. The reconstructed spatial resolution was 12-mm full-width at half-maximum (FWHM) using this reconstruction procedure. The dynamic data for the conventional sampling schedules consisted of fifteen 60-s scans, nine 300-s scans, and twelve 600-s scans. The Logan [8] and Yokoi [10] graphical methods were applied to the voxel-by-voxel TTACs from the conventional sampling schedule data to derive parametric images for  $V_d$  and  $K_1$ , respectively. For the integrated method, application of

OISS to the dynamic data for a four parameter model resulted in four frames with durations of 7.3, 21.8, 81.3, and 69.7 min [19]. Cluster analysis was performed on the reconstructed OISS frames and the cluster TTAC were fitted with GLLS to generate the voxel-by-voxel parametric images for the integrated method. The GLLS method was also applied to each voxel TTAC without prior clustering for CSS and OISS to determine the effect of sampling schedule and clustering on the results. To avoid discrepancies of parameter estimates due to different underlying kinetic models,  $K_1$  was estimated by the GLLS method for two-compartment and two-parameter model in line with the underlying model assumed by the Yokoi graphical method. Similarly, a three-compartment and four-parameter model was used with GLLS to estimate  $V_d$  in line with the underlying model assumed by the Logan method.

Tight volumes of interest (VOI) were defined for the cerebellum, thalamus and frontal cortex from the definition of the mathematical human brain phantom. Twenty dynamic simulation data sets were generated for each of the five noise levels. Percentage bias for each VOI applied to the generated parametric images was calculated according to (7) to evaluate the accuracy of the obtained voxel-wise parametric images. Coefficient of variations (CV) (8) across the 20 simulation data sets were also derived to compare the reliability of the obtained parametric images

$$\text{Bias} = \frac{\frac{1}{M} \left[ \sum_{i=1}^M \sum_{j=1}^N \frac{p_{i,j} - p_0}{N} \right]}{p_0} \times 100\% \quad (7)$$

$$\text{CV} = \frac{\sqrt{\frac{\sum_{i=1}^M \left( \sum_{j=1}^N \frac{p_{i,j}}{N} \right)^2 - M \left( \sum_{i=1}^M \sum_{j=1}^N \frac{p_{i,j}}{N} \right)^2}{M-1}}}{p_0} \times 100\% \quad (8)$$

In (7) and (8),  $p_{i,j}$  is the estimated parameter for the  $j$ th voxel in the corresponding VOI for the  $i$ th simulation data set,  $p_0$  is the reference value,  $M$  is the number of simulation data sets for each of noise levels, and  $N$  is the total number of voxels for the VOI.

### C. Evaluation of Partial Volume Effects

To evaluate the impact of partial volume effect on the parametric image derived by the integrated method, five digital phantoms with spherical hot lesions of various sizes were simulated. The cylindrical phantom consisted of a 140-mm-diameter, 140-mm-long cylinder. An outer, 10-mm-thick rim was assumed to have the kinetics of the frontal cortex and the remaining 120-mm-diameter central cylinder was assigned as white matter. Five hot spheres, whose diameters varied from 10 mm to 50 mm, were located in the center of each phantom with the kinetics of the thalamus.

Projection data sets were simulated, processed, and reconstructed as described for the brain phantom studies above. Parametric images were derived by the Logan and Yokoi graphical methods for CSS and OISS data sets, as well as by the GLLS method with cluster analysis. The percentage bias and CV of  $K_1$  and  $V_d$  were estimated for spherical VOIs, which were derived by eroding the known volumes of the spheres with two-voxel wide masks.

#### D. SPECT Studies Analysis

Seven SPECT studies with the neuronal nicotinic acetylcholine receptor tracer 5- $^{123}\text{I}$ -iodo-A-85380 were acquired in two adult male Papio hamadryas baboons. The studies were approved by the Central Sydney Area Health Service animal welfare committee. All studies were carried out on a Triad XLT triple head gamma camera (Trionix Research Laboratories, Twinsburg, OH). Prior to administration of the tracer, a transmission study was collected for 15 min with a line source containing  $^{99\text{m}}\text{Tc}$  at the focal line of a long focal distance (1140 mm) fan beam collimator. Emission dynamic SPECT scanning was performed with UHR short focal length (480 mm) fan beam collimators attached to all three detectors. Scanning and arterial blood sampling commenced at the start of a 2-min infusion of  $397 \pm 43$  MBq of the tracer. Total acquisition time extended over 3 hrs and frame rate was the same as that detailed for the simulations. The emission data ( $128 \times 64$  matrix  $\times 60$  angles per frame) were corrected using transmission dependent scatter correction [2], [3], [27] and reconstructed using OS-EM with 20 subsets and two iterations, with a zoom of  $\times 1.6$  (reconstructed voxel size  $2.2 \text{ mm} \times 2.2 \text{ mm} \times 2.2 \text{ mm}$ ).

As for the simulations, parametric images were estimated with the Logan ( $V_d$ ) and Yokoi ( $K_1$ ) methods using the conventional sampling scheme data and the measured input function. Parametric images of  $V_d$  and  $K_1$  were also estimated with the integrated method. Results from the graphical methods were compared with the integrated method by linear regression analysis of parameters derived from manually defined regions applied to the parametric images.

### III. RESULTS

#### A. Evaluation of Computer Simulation

The line source profiles, obtained from the experimental measurements and Monte Carlo simulations were scaled to the same maximum counts, are plotted in Fig. 2 for source to detector distance of 100 mm in air [Fig. 2(a)] and source to detector distance of 200 mm with 100 mm water scatter medium [Fig. 2(b)]. There is reasonable agreement between simulation and experimental data for both the line source and background counts from scatter and the contributions from septal penetration of the high energy emissions of  $^{123}\text{I}$ . Similar results were observed in the other three studies, with detector distances of 50, 150, and 200 mm. Thus, the simulation data are considered sufficiently realistic for the purpose and aims of this study.

#### B. Percentage Bias

Fig. 3 shows the percentage bias for the frontal cortex at various noise levels. Fig. 4 summarizes bias as a function of CVs for all noise levels for the frontal cortex as well as the other structures investigated. Despite of the lowest bias achieved for the noise free data, the estimation of  $K_1$  with the Yokoi method from CSS data was most affected by noise, with the other techniques being relatively insensitive to the levels of noise. Overall, except for the noise-sensitive Yokoi method, GLLS with OISS and the integrated method showed the lowest bias for  $K_1$  [Fig. 4(a) and (b)]. In the cerebellum, the integrated method suffered from higher bias of  $K_1$  compared with GLLS

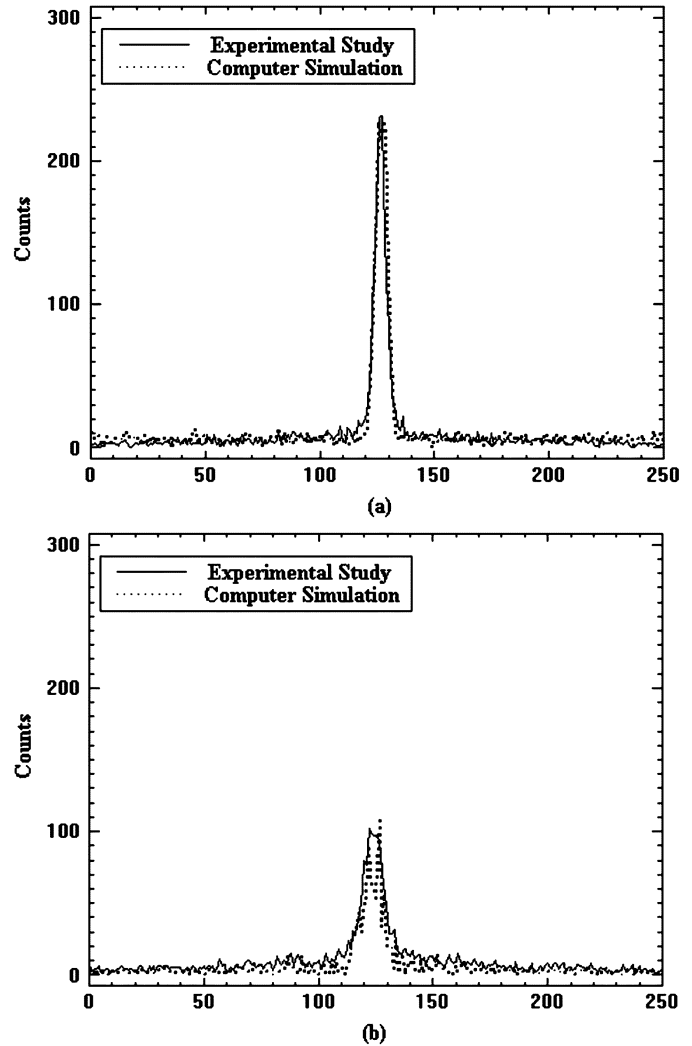


Fig. 2. Profile plots through line source projection images for the experimental study versus computer simulation. Solid line: Experimental study, Dotted line: Computer simulation. (a) Detector distance is 100 mm. (b) Detector distance is 200 mm with 100 mm of water scatter interposed between the line source and the detector.

with OISS [Fig. 4(c)]. The higher bias with the integrated method in the cerebellum may be due to the particular curve shapes of voxel cluster centroid TTACs being affected by partial volume effects and spill over in the cerebellum and the higher weights given to the longer, late frames with clustering adversely influencing the early part of the clustered curve.  $K_1$  is most affected by the early parts of the curve and hence the higher bias in  $K_1$ , but not  $V_d$  which is governed more by the late curve points.

The integrated method displayed the least sensitivity of  $V_d$  bias to noise and overall showed the lowest bias of all the methods investigated [Figs. 3 and 4]. There was a strong influence of noise on the bias of  $V_d$  estimates when GLLS was applied without clustering (OISS-GLLS and CSS-GLLS) in Figs. 3 and 4(d)–(f). Only the bias of the integrated method was largely unaffected by noise. The positive bias of  $V_d$  by integrated method in cerebellum confirmed that the weighted least-square distance measure in clustering may potentially decrease early points' and increase late points'

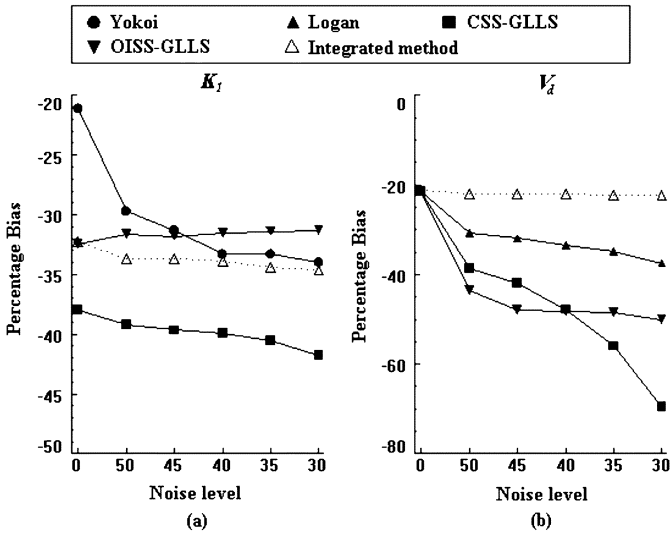


Fig. 3. Plots of percentage bias for frontal cortex as the function of increasing noise level in the projections (the number value denotes maximum pixel count for a 5-min frame except 0 represents noise free data). Yokoi—Yokoi graphical method. Logan—Logan graphical method. CSS-GLLS—GLLS applied to CSS data without clustering. OISS-GLLS—GLLS applied to OISS data without clustering. Integrated method—the proposed integrated method i.e., GLLS applied to clustered OISS data.

activity values for this particular structure and is in line with the more pronounced underestimation of  $K_1$  in cerebellum by the integrated method.

### C. Coefficient of Variation

CVs for the frontal cortex are plotted in Fig. 5 as a function of noise level. As is evident from Figs. 4 and 5, the CVs of  $K_1$  are small ( $<5\%$ ) for all structures, methods and noise levels except the Yokoi method, which achieved the highest CV, with a thalamus CV of 9.2% at the highest noise level. The strategies used to reduce the effect of noise (OISS and clustering) did not improve the reliability of  $K_1$  estimates, but this is of little consequence given the already low CVs and hence good reliability. In contrast, the noise reduction strategies for GLLS did have a marked effect on the reliability of  $V_d$  estimates with CV values decreasing by including OISS and a further decrease in CV was achieved by clustering as used in the integrated method (Figs. 4 and 5). An acceptable  $V_d$  reliability is achieved with the integrated method for all structures and noise levels, while the Logan graphical method overall provided the most reliable estimates of  $V_d$ .

It is not entirely unexpected that the Yokoi method yielded lowest bias for estimation  $K_1$ , as fitting of the Yokoi curve was restricted to the linear part of the curve covering the first 20 min of data. These early frames, while strongly influenced by flow, have very low SNR giving rise to the overestimation of  $K_1$ , as well as high CVs. When the Yokoi method was applied to the late part of the curve, CV was reduced to be in line with the other techniques, but bias was then the worst of all the techniques.

### D. Partial Volume Effect

Fig. 6 depicts the percentage bias as a function of sphere diameters of the hot lesions at the highest level of noise. As ex-

pected, underestimation of parameters generally increased with decreasing sphere diameter due to partial volume effect and became very pronounced with biases exceeding  $-70\%$  for  $K_1$  and  $-80\%$  for  $V_d$  for the 10-mm diameter lesion which is smaller than the approximately 12-mm FWHM resolution of the simulated camera system. For  $K_1$ , the methods not including clustering had very similar bias and trends as a function of sphere diameter (Fig. 6). Interestingly, when clustering was included, the bias due to partial volume effect was reduced and less affected by sphere diameter, becoming only pronounced at the smallest sphere diameter of 10 mm.

For estimating  $V_d$ , clustering also reduced the partial volume effect for all sphere diameters, although in this case the effect of decreasing sphere diameter on bias was more pronounced for the clustered results than observed for  $K_1$ . Interestingly, the Logan graphical method applied to OISS data showed the least bias for  $V_d$ , which may be due to the limited number of only 4 frames for OISS making it difficult to identify a region where  $Con$  in (4) is constant and fortuitously resulting in a higher slope and hence less biased  $V_d$ .

The slope of bias versus sphere diameter for  $V_d$  is larger with clustering than without clustering, suggesting that PVE has a more pronounced effect when clustering is employed. However, this is considered an artifact, as without clustering, there are a large number of unsuccessful fits, given a very high bias at even the largest sphere diameter, and this high bias persists to lower sphere diameters, thus the incremental increase in bias with decreasing sphere diameter is correspondingly less. As is evident from Fig. 6, the bias with clustering was less than that for the corresponding method without clustering for all sphere diameters. This reduction in bias is attributed to clustering reducing or eliminating the number of unsuccessful fits, with corresponding reduction in bias.

For a given structure, voxels at the periphery of the structure will be affected more by PVE than those at the center, hence peripheral voxels will have larger bias. Without clustering, the estimated bias for the structure is the average bias of biases over the structure (high at the periphery, lower at the center). With approximately 150 clusters being generated during the cluster analysis, a particular structure will include multiple clusters such as clusters representing peripheral, intermediate, and central structure voxels. Bias will then be determined by the average of the bias for each cluster representing the structure. Thus, clustering should not introduce more pronounced PVE and may in fact reduce it by eliminating contributions from high bias, outlier voxels.

### E. Parametric Images From Simulation Data

Representative examples of the parametric images generated from the simulation brain data are shown in Fig. 7 at the highest noise level. While the VOI mean parameter values for the Yokoi method did not appear to be excessively affected by noise (Figs. 3–5), the parametric images generated by the Yokoi method demonstrated very high levels of noise, which resulted in some unreasonable high values as shown in Fig. 7(a) and a large number of outliers to degrade the parametric images to such an extent that they are uninterpretable. In contrast,  $V_d$  images generated by the Logan method do not demonstrate

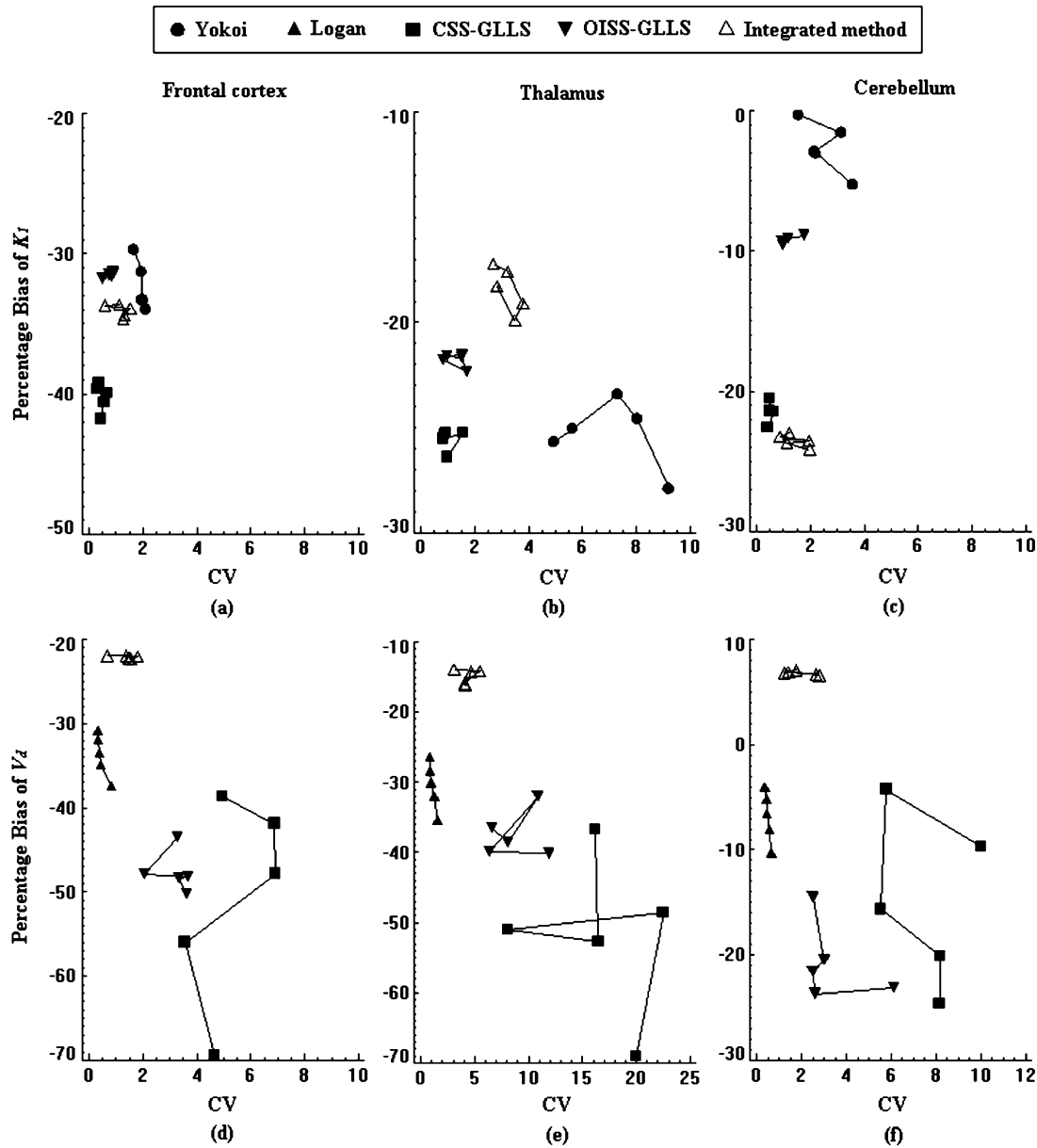


Fig. 4. Plots of percentage bias for increasing noise levels as a function of coefficient of variation. (a) Percentage bias versus CV of  $K_1$  for frontal cortex. (b) Percentage bias versus CV of  $K_1$  for thalamus. (c) Percentage bias versus CV of  $K_1$  for cerebellum. (d) Percentage bias versus CV of  $V_d$  for frontal cortex. (e) Percentage bias versus CV of  $V_d$  for thalamus. (f) Percentage bias versus CV of  $V_d$  for cerebellum. Legends are the same as for Fig. 3.

a high level of noise and appear quite smooth [Fig. 7(b)]. Fig. 7(c) and (d) presents the parametric images obtained by integrated method for  $K_1$  and  $V_d$ . There is a very clear reduction in noise of the  $K_1$  parametric image with the integrated method [Fig. 7(c)] compared to the graphical Yokoi method [Fig. 7(a)]. Structures are clearly identifiable with the integrated method, but buried in noise with the graphical method. For  $V_d$ , the improvement in noise with the integrated method is less pronounced. However, overall the cortex and particularly the thalamus are better defined with the integrated method [Fig. 7(d)] than with the Logan method [Fig. 7(b)] as illustrated by the more regular outline of the thalamus with the integrated method and presence of dark, artificial defects in the thalamus with the Logan method, which are absent from the integrated method parametric images.

F. Baboon Studies

VOIs were defined on the dynamic reconstructed data from the conventional sampling scheduled for the cerebellum, thalamus, and frontal cortex, and superimposed on the parametric images generated by the methods under investigation. The mean parameter values derived from the VOIs for the integrated method are plotted against the corresponding values for the graphical techniques in Fig. 8. Fig. 9 shows a comparison of parametric images derived by the various methods for one of the baboon studies.

The correlation coefficient between the Yokoi and integrated method for  $K_1$  was low at 0.214 [Fig. 8(a)]. This poor agreement seen in Fig. 8(a) is attributed to the high levels of noise and unreliable fits with the Yokoi method [Fig. 9(a)]. In contrast, the

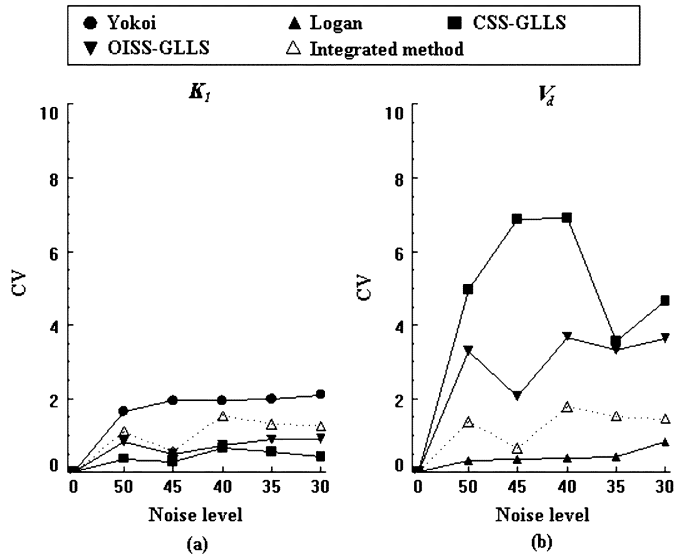


Fig. 5. Plots of coefficient of variation for the frontal cortex as a function of increasing noise level in the projections. Legends are the same as for Fig. 3.

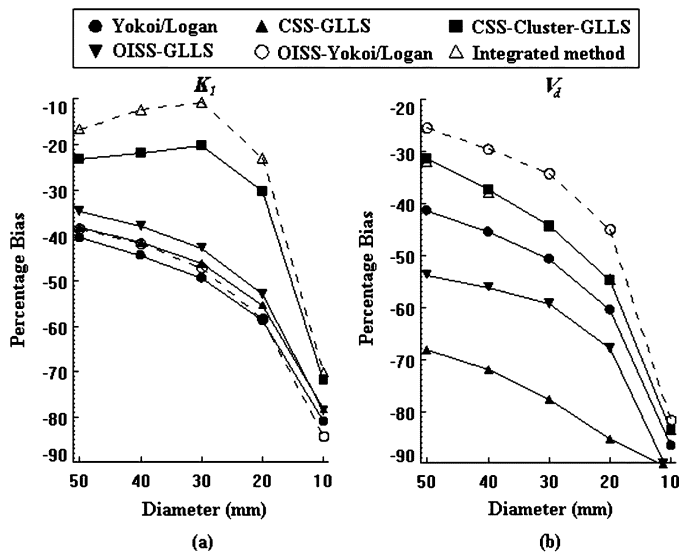


Fig. 6. Plots of percentage bias as a function of hot spheres diameters. Yokoi/Logan—Yokoi or Logan method applied to CSS data. CSS-GLLS—GLLS applied to CSS data without clustering. CSS-Cluster-GLLS—GLLS applied to clustered CSS data. OISS-GLLS—GLLS applied to OISS data without clustering. OISS-Yokoi/Logan—Yokoi or Logan methods applied to OISS data. Integrated method—GLLS applied to clustered, OISS data.

results for  $V_d$  were highly correlated with a correlation coefficient of 0.943 [Fig. 8(b)]. The values of the integrated method tended to be higher than those estimated by the Logan method (slope = 1.5), which provides further evidence that the clustering employed by the integrated method does not suffer from more bias due to partial volume effects.

The parametric images generated by the Yokoi method [Fig. 9(a)] are uninterpretable due to the high noise level and large number of unsuccessful fits. Successful fits and interpretable results are achieved with the integrated method for  $K_1$ , as shown in Fig. 9(c). Both the Logan graphical method and the integrated method achieved low noise, interpretable parametric images of  $V_d$ . However, through clustering, the

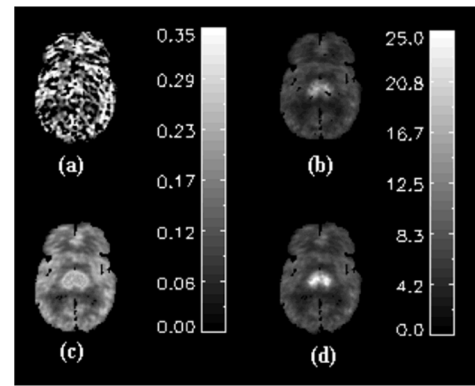


Fig. 7. Parametric images for  $K_1$  and  $V_d$  for the highest level of noise. (a)  $K_1$  by Yokoi plot. (b)  $V_d$  by Logan plot, (c)  $K_1$ . (d)  $V_d$  by the integrated method.

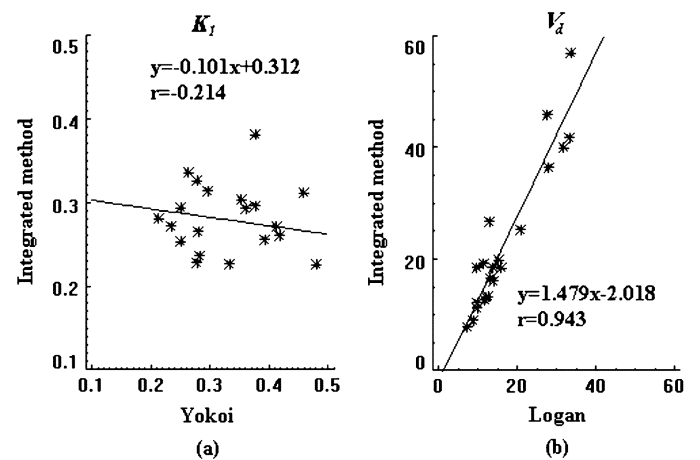


Fig. 8. Plots of the mean parameter obtained by Logan and Yokoi approaches against the integrated method. (Seven studies and three ROI).

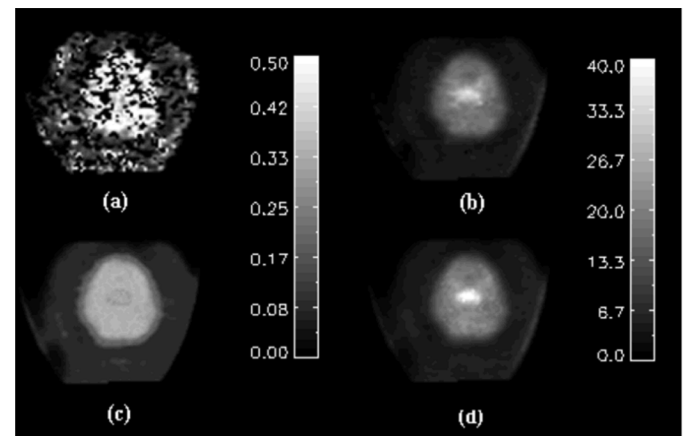


Fig. 9. Parametric images for  $K_1$  and  $V_d$  for one baboon study. (a)  $K_1$  by Yokoi plot. (b)  $V_d$  by Logan plot. (c)  $K_1$ . (d)  $V_d$  by the integrated method.

delineation of the thalamus is clearer and more pronounced with the integrated method [Fig. 9(d)] than with the Logan graphical method [Fig. 9(b)].

#### IV. DISCUSSION

GLLS is a well-established method for solving linear compartment models with fast computational speed. However, the



high level of noise in dynamic SPECT can give rise to unsuccessful fits to some TTACs even with a large number of iterations. In this study, we have thus proposed a new integrated method for generating parametric images from dynamic SPECT studies with their associated high levels of noise, while still being able to take advantage of the computational efficiency and versatility afforded by GLLS. Noise reduction in the integrated method is achieved by incorporating two strategies. First, noise in the temporal domain is reduced by combining the short duration, high noise frames of conventional sampling schedules into the minimum number of longer duration frames required to estimate the parameters of interest using the OISS methodology. Second, cluster analysis is employed to reduce noise in the spatial domain of the reconstructed data as the noisy individual voxel TTACs are replaced by the most similar centroid TTAC which is formed from the mean of the TTACs contributing to the corresponding cluster.

Graphical methods such as Patlak, Logan, and Yokoi plots are also computationally highly efficient in generating parametric images but do rely on underlying assumptions, models and restrictions [30]. GLLS allows estimation of the rate constants for the most appropriate model for the tracer and hence estimation of a range of macro parameters, including  $V_d$  and binding potential. In contrast, graphical techniques provide only a select few parameters and estimation of, for example, binding potential is limited to tracers where a reference tissue devoid of the receptors of interest can be defined [31]. For the tracer under investigation in this study, no reference tissue is available, so comparison of GLLS with graphical methods was limited to the parameters which could be estimated by the graphical methods using the plasma input function.

The success of the strategies, involved in the integrated method, to reduce the effect of noise is particularly evident in the parametric images shown in Figs. 7 and 9. The parametric images of  $K_1$ , derived by the integrated method [Figs. 7(c) and 9(c)], were superior to those by the Yokoi method for the simulation data Fig. 7(a) and baboon data Fig. 9(a), particularly in terms of noise. The Yokoi graphical plot was not linear over the entire collection time period. Thus, the linear region covering the first 20 min of data was selected for fitting the Yokoi equations. While this resulted in the least biased  $K_1$ , this was at the expense of very high noise. Fitting the Yokoi equation to late time points resulted in bias substantially worse than that by the integrated method, and noise, while substantially reduced, still visually worse than that seen by the integrated method. For a fair comparison with the Yokoi method, whose model is assumed to be two compartments and two parameters,  $K_1$  was estimated by the integrated method using a two-compartment model as well. However, when estimating  $K_1$  with the integrated method and a more appropriate three-compartment model for the observed kinetics, the bias of  $K_1$  was further reduced due to the better description of the tracer kinetics, e.g., percentage bias of  $-24.6\%$  for frontal cortex at the highest noise level, compared  $-34.7\%$  for the two-compartment model. Thus flexible choice of the proper kinetic model for the GLLS method is beneficial to the parameter estimates in quantitative functional studies, while the Yokoi approach is restricted to the simple two-compartment model. This is also in line with

the underestimation of parameters by the graphical methods compared to three-compartment model NLLS fits previously observed [28].

The integrated method also compared favorably with the Logan method in the estimation of  $V_d$ . Overall the integrated method produced slightly less bias than the Logan method applied to CSS data. While CVs of  $V_d$  for the integrated method were somewhat higher than those observed with the Logan method (Figs. 4 and 5), they were still less than 5% for all structures and noise levels. The parametric images generated by the integrated method appear to overall be less affected by noise compared with those generated by the Logan method (Figs. 7 and 9). However, both techniques produce very acceptable results for estimating parametric images of  $V_d$ .

The versatility and flexibility of selecting the most appropriate model and parameters of GLLS come at the expense of higher sensitivity to noise. GLLS with CSS suffered from large CV values, particularly for estimating  $V_d$  (Figs. 4 and 5) at the higher noise levels and increasing and high bias with increasing noise. The high bias at high noise levels is largely attributed to the number of successfully fitted voxels in the parametric images decreasing with increasing noise. Voxels with unsuccessful fits were set to zero, hence increasing bias as less and less voxels are fitted successfully. From the results, it is clear that both strategies for reducing noise (OISS and clustering) lead to improvements in the parameter estimates. This is highlighted in Fig. 4, for  $V_d$ , where GLLS applied to CSS data (CSS-GLLS) demonstrated the highest bias, with reduction in bias seen by employing OISS (OISS-GLLS) or clustering (CSS-Cluster-GLLS) on their own, but with the largest reduction in bias seen when both techniques are used in combination (Integrated method).

An underlying assumption of cluster analysis is that the number of observed kinetics in the data is finite. Due to partial volume effects, many voxels may contain a mixture of TTACs from different structure due to spill-in and spill-out, which thus may violate the assumptions of limited number of underlying kinetics. When these mixed voxels contribute and are assigned to particular structures, they may theoretically increase the bias due to partial volume effects. Rather than relying on a fixed number of predefined clusters, the clustering approach taken for the integrated method relies on automatically determined cluster centroids and cluster numbers. The number of clusters formed is then largely governed by the threshold  $\Delta d$  (4), which determines whether a given TTAC is close enough to any of the existing cluster centroid TTACs to be assigned to an existing cluster or whether a new cluster will need to be formed. With the selected threshold value, the number of clusters was insensitive to the level of noise, with  $149 \pm 5$  clusters being formed for the lowest level of noise,  $148 \pm 5$  for the moderate level of noise,  $149 \pm 6$  for the highest level of noise. The number of clusters is large enough to adequately account for and characterize the kinetics of "mixed" voxels with contributions from multiple structures.

No corrections were applied for partial volume effects caused by the limited spatial resolution in the data. Thus underestimation of parameters is expected by all techniques particularly for small structures such as the thalamus or the 10-mm-diameter

sphere. As is evident from the results, the application of clustering did not overall increase bias due to partial volume effects. On the contrary, bias appears to be overall reduced and sensitivity of bias to noise is largely eliminated. Only for estimating  $K_1$  in the cerebellum, did GLLS with OISS, but without clustering show a markedly decreased bias compared to the integrated method. As indicated above, this is attributed to the particular shape of the TTACs in the cerebellum and the relative weights given to frames during clustering and warrants further investigation.

To remove the remaining bias, partial volume correction would need to be applied. The focus of this paper was to compare the integrated method against established graphical methods in the generation of parametric images and to evaluate the contributions of the noise reduction strategies (OISS and clustering) to the performance of the integrated method. Thus evaluation of different partial volume correction techniques, which may remove the remaining bias, was considered outside the scope of this paper.

OISS depends on the particular kinetics observed, and theoretically may differ between different structures showing differences in kinetics. For this study, the cost function (1) was optimized for a combination of different kinetics observed in various structures for this tracer. The exact frame duration for OISS is not critical even for different cameras or different curve fit methods, and the same frame rate can be applied for a range of different kinetics, so OISS does not have to be separately determined for different structures or studies [32].

The dynamic SPECT data were reconstructed with iterative reconstruction which allowed correction for attenuation and scatter. The number of dynamic SPECT frames which needed to be reconstructed was reduced from 36 frames for CSS to only four frames required for OISS to allow fitting of the three-compartment model, resulting in a substantial reduction in reconstruction time. Combined with the small number of cluster centroids derived by cluster analysis and fast estimation of GLLS, the integrated method proved computationally very efficient in generating parametric images. For instance, it took approximately 2.2 h for the integrated method to derive the 20 sets of parametric images at one level of noise including the reconstruction on a SUN blade-2000 workstation (two 1.015-GHz CPUs, 512 MB of memory). This was about five times faster than the graphical methods, which took about 11 h to generate the same 20 sets of parametric images for the conventional sampling schedule.

## V. CONCLUSION

An integrated method was developed and evaluated to allow parametric images to be successfully generated with GLLS from noisy SPECT data. The strategies employed to reduce noise include noise reduction in the temporal domain by employing OISS and reduction in the spatial domain through clustering. The simulations and experimental studies demonstrate that the integrated method can successfully generate low-noise parametric images, without undue adverse effects on the bias. The application of this method was computationally sufficiently fast for potential clinical application. The proposed

method can potentially be extended to other kinetic models and tracers.

## REFERENCES

- [1] K. J. LaCroix, B. M. W. Tsui, B. H. Hasegawa, and J. K. Brown, "Investigation of the use of X-Ray CT images for attenuation compensation in SPECT," *IEEE Trans. Nucl. Sci.*, vol. 41, no. 6, pp. 2793–2799, Dec. 1994.
- [2] S. R. Meikle, B. F. Hutton, and D. L. Bailey, "A transmission-dependent method for scatter correction in SPECT," *J. Nucl. Med.*, vol. 35, no. 2, pp. 360–367, Feb. 1994.
- [3] Y. Narita, S. Eberl, H. Iida, B. F. Hutton, M. Braun, T. Nakamura, and G. Bautovich, "Monte Carlo and experimental evaluation of accuracy and noise properties of two scatter correction methods for SPECT," *Phys. Med. Biol.*, vol. 41, no. 11, pp. 2481–2496, Nov. 1996.
- [4] P. Almeida, M. J. Ribeiro, M. Bottlaender, C. Loc'h, O. Langer, D. Strul, P. Hugonnard, P. Grangeat, B. Mazière, and B. Bendriem, "Absolute quantitation of iodine-123 epidepride kinetics using single-photon emission tomography: Comparison with carbon-11 epidepride and positron emission tomography," *Eur. J. Nucl. Med.*, vol. 26, no. 12, pp. 1580–1588, Dec. 1999.
- [5] M. Ichise, J. H. Meyer, and Y. Yonekura, "An introduction to PET and SPECT neuroreceptor quantifications models," *J. Nucl. Med.*, vol. 42, pp. 755–763, 2001.
- [6] M. Ichise, J. R. Ballinger, H. Golan, D. Vines, A. Luong, S. Tsai, and H. F. Kung, "Noninvasive quantification of dopamine D2 receptors with iodine-123-IBF SPECT," *J. Nucl. Med.*, vol. 37, pp. 513–520, 1996.
- [7] C. S. Patlak, R. G. Blasberg, and J. D. Fenstermacher, "Graphical evaluation of blood-to-brain transfer constants from multiple-time uptake data," *J. Cereb. Blood Flow Metab.*, vol. 3, pp. 1–7, 1983.
- [8] J. Logan, J. S. Fowler, N. D. Volkow, A. P. Wolf, S. L. Dewey, D. J. Schlyer, R. R. MacGregor, R. Hitzemann, B. Bendriem, S. J. Gatley, and D. R. Christman, "Graphical analysis of reversible radioligand binding from time-activity measurements applied to [ $N$ - $^{11}$ C-methyl]-(-)-Cocaine PET studies in human subjects," *J. Cereb. Blood Flow Metab.*, vol. 10, pp. 740–747, 1990.
- [9] J. Logan, J. S. Fowler, N. D. Volkow, G.-J. Wang, Y. S. Ding, and D. L. Alexoff, "Distribution volume ratios without blood sampling from graphical analysis of PET data," *J. Cereb. Blood Flow Metab.*, vol. 16, pp. 834–840, 1996.
- [10] T. Yokoi, H. Iida, H. Itoh, and I. Kanno, "A new graphic plot analysis for cerebral blood flow and partition coefficient with Iodine-123-Iodoamphetamine and Dynamic SPECT validation studies using Oxygen-15-water and PET," *J. Nucl. Med.*, vol. 34, no. 3, pp. 498–505, Mar. 1993.
- [11] D. Feng, S. C. Huang, Z. Wang, and D. Ho, "An unbiased parametric imaging algorithm for nonuniformly sampled biomedical system parameter estimation," *IEEE Trans. Med. Imag.*, vol. 15, no. 4, pp. 512–518, Aug. 1996.
- [12] K. Chen, M. Lawson, E. Reiman, A. Cooper, D. Feng, S. C. Huang, D. Bandy, D. Ho, L. Yun, and A. Palant, "Generalized linear least squares method for fast generation of myocardial blood flow parametric images with N-13 Ammonia PET," *IEEE Trans. Med. Imag.*, vol. 17, no. 2, pp. 236–243, Apr. 1998.
- [13] K. P. Wong, D. Feng, and W. C. Siu, "Generalized linear least squares algorithm for non-uniformly sampled biomedical system identification with possible repeated eigenvalues," *Comput. Meth. Programs Biomed.*, vol. 57, no. 3, pp. 167–177, Nov. 1998.
- [14] R. A. Hawkins, M. E. Phelps, and S. C. Huang, "Effects of temporal sampling, glucose metabolic rates, and disruptions of the blood-brain barrier on the FDG model with and without a vascular compartment: Studies in human brain tumours with PET," *J. Cereb. Blood Flow Metab.*, vol. 6, pp. 170–183, 1986.
- [15] J. Delforge, A. Syrota, and B. M. Mazoyer, "Experimental design optimization: Theory and application to estimation of receptor model parameters using dynamic positron emission tomography," *Phys. Med. Biol.*, vol. 34, pp. 419–435, 1989.
- [16] X. Li, D. Feng, and K. Chen, "Optimal image sampling schedule: A new effective way to reduce dynamic image storage space and functional image processing time," *IEEE Trans. Med. Imag.*, vol. 15, no. 5, pp. 710–719, Oct. 1996.
- [17] X. Li and D. Feng, "Towards the reduction of dynamic image data in positron emission tomography studies," *Comput. Meth. Programs Biomed.*, vol. 53, no. 2, pp. 71–80, Jun. 1997.

- [18] X. Li, D. Feng, and K. P. Wong, "A general algorithm for optimal sampling schedule design in nuclear medicine imaging," *Comput. Meth. Programs Biomed.*, vol. 65, no. 1, pp. 45–59, Apr. 2001.
- [19] L. Wen, S. Eberl, D. Feng, and J. Bai, "An improved optimal image sampling schedule for multiple ROIs in dynamic SPECT," in *Modeling and Control in Biomedical Systems 2003*, D. Feng and E. Carson, Eds. Oxford, U.K.: Elsevier, 2003, pp. 139–143.
- [20] Y. Kimura, H. Hsu, H. Toyama, M. Senda, and N. M. Alpert, "Improved signal-to-noise ratio in parametric images by cluster analysis," *NeuroImage*, vol. 9, no. 5, pp. 554–561, May 1999.
- [21] Y. Kimura, M. Senda, and N. M. Alpert, "Fast formation of statistically reliable FDG parametric images based on clustering and principal components," *Phys. Med. Biol.*, vol. 47, no. 3, pp. 455–468, Feb. 7, 2002.
- [22] K. P. Wong, D. Feng, S. R. Meikle, and M. J. Fulham, "Segmentation of dynamic PET images using cluster analysis," *IEEE Trans. Nucl. Sci.*, vol. 49, no. 1, pp. 200–207, Feb. 2002.
- [23] A. Simmons, S. R. Arridge, G. J. Barker, and S. C. R. Williams, "Simulation of MRI cluster plots and application to neurological segmentation," *Magn. Reson. Imag.*, vol. 14, no. 1, pp. 73–92, 1996.
- [24] A. J. Sims, M. K. Bennett, and A. Murray, "Comparison of semi-automated image analysis and manual methods for tissue quantification in pancreatic carcinoma," *Phys. Med. Biol.*, vol. 47, no. 8, pp. 1255–1266, Apr. 21, 2002.
- [25] T. K. Lewellen, R. L. Harrison, and S. Vannoy, "The Simset Program," in *Monte Carlo Calculations in Nuclear Medicine*, ser. Medical Science Series, M. Liungberg, S. E. Strand, and M. A. King, Eds. Bristol, U.K.: Inst. Phys. Publishing, 1998, pp. 77–92.
- [26] I. G. Zubal, C. R. Harrell, E. O. Smith, Z. Rattner, G. Gindi, and P. B. Hoffer, "Computerized 3-dimensional segmented human anatomy," *Med. Phys.*, vol. 21, pp. 299–302, 1994.
- [27] H. Iida, Y. Narita, H. Kado, A. Kashikura, S. Sugawara, Y. Shoji, T. Kinoshita, T. Ogawa, and S. Eberl, "Effects of scatter and attenuation correction on quantitative assessment of regional cerebral blood flow with SPECT," *J. Nucl. Med.*, vol. 39, no. 1, pp. 181–189, Jan. 1998.
- [28] M. Kassiou, S. Eberl, S. R. Meikle, A. Birrell, C. Constable, M. J. Fulham, D. F. Wong, and J. L. Musachio, "In vivo imaging of nicotinic receptor upregulation following chronic (-)-nicotine treatment in baboon using SPECT," *Nucl. Med. Biol.*, vol. 28, pp. 165–175, 2001.
- [29] H. M. Hudson and R. S. Larkin, "Accelerated image reconstruction using ordered subsets of projection data," *IEEE Trans. Med. Imag.*, vol. 13, no. 4, pp. 601–609, Dec. 1994.
- [30] J. Logan, "Graphical analysis of PET data applied to reversible and irreversible tracers," *Nucl. Med. Biol.*, vol. 27, pp. 661–670, 2000.
- [31] M. Ichise, J. S. Liow, J. Q. Lu, T. Takano, K. Model, H. Toyama, T. Suhara, K. Suzuki, R. B. Innis, and R. E. Carson, "Linearized reference tissue parametric Imaging methods: Application to [<sup>11</sup>C]DASB positron emission tomography studies of the serotonin transporter in human brain," *J. Cereb. Blood Flow Metab.*, vol. 23, no. 9, pp. 1096–1112, Sept. 2003.
- [32] C. H. Lau, S. Eberl, D. Feng, H. Iida, P. K. Lun, W. C. Siu, Y. Tamura, G. J. Bautovich, and Y. Ono, "Optimized acquisition time and image sampling for dynamic SPECT of Tl-201," *IEEE Trans. Med. Imag.*, vol. 17, no. 3, pp. 334–343, Jun. 1998.